Supplementary Information: Integrated on-chip quantum light sources on a van der Waals platform

Pietro Metuh,[1] Paweł Wyborski,[1] Athanasios Paralikis,[1] Frederik Schröder,[1,2] Nicolas Stenger,[1,2] Niels Gregersen,[1] and Battulga Munkhbat[1,*]

[1] *Department of Electrical and Photonics Engineering, Technical University of Denmark, 2800 Kgs. Lyngby, Denmark*
[2] *NanoPhoton – Center for Nanophotonics, Technical University of Denmark, 2800 Kgs. Lyngby, Denmark*

Contents

* bamunk@dtu.dk

Supplementary Note 1: Additional nanofabrication and imaging details

This section includes additional optical microscopy and scanning electron microscopy images illustrating the fabrication process of WS_2 optical waveguides. As described in the Methods section of the main text, we begin by selecting a WS_2 flake with suitable thickness and homogeneity, such as the one shown in Supplementary Fig. 1a, after exfoliating them on PDMS stamps. Having measured the reflectivity and determined the thickness of the flake via the transfer-matrix method, the flake is released on a Si/SiO_2 substrate with pre-patterned alignment marks. A profilometry scan (Supplementary Fig. 1b) confirms the thickness measured with the transfer-matrix method. The WS_2 structures are then patterned by preparing a resist mask (Supplementary Fig. 1c) and processing the sample with reactive-ion etching (Supplementary Fig. 1d). At this point, the resist is removed with an oxygen plasma, revealing the WS_2 waveguides (Fig.s 1e-f).

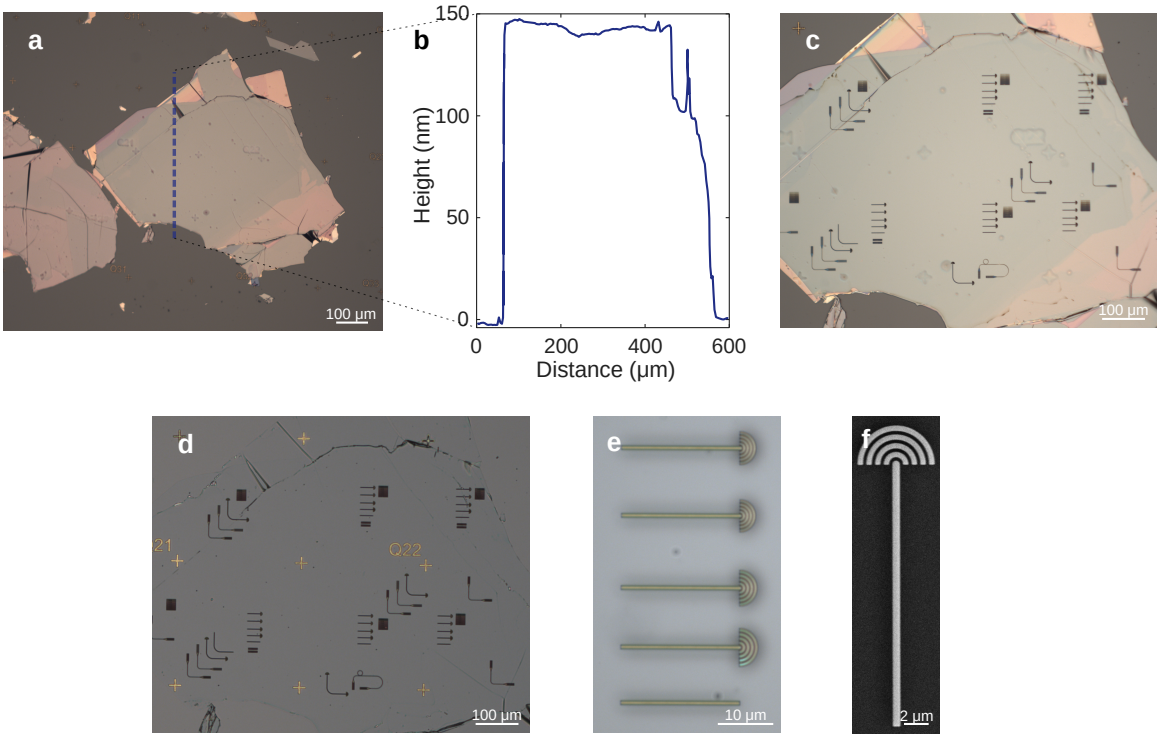

Supplementary Fig. 1. Nanofabrication of WS_2 waveguides. (a) Optical microscopy image of a WS_2 flake used for the emitter-integrated samples presented in the main text, after transferring on a Si/SiO_2 substrate. (b) Profilometry scan along the dashed line in (a), showing an approximate thickness of 150 nm. (c) Optical microscopy image after resist development, revealing the structure pattern on the flake. (d) Optical microscopy image after the reactive-ion etching and resist stripping steps. (e) Magnified optical microscopy image of short WS_2 waveguides. (f) Scanning electron microscopy image of the waveguide characterized with near-field optical microscopy.

Supplementary Note 2: Additional data on the WS_2 photonic devices

Scattering-type scanning near-field optical microscopy data. Figure 2f of the main text illustrates the dispersion relation obtained when exciting a WS_2 waveguide under variable excitation wavelength (1120–1190 nm). Here, we show the raw data used to extract such dispersion relation. Supplementary Figure 2a shows an enlarged view of the atomic force microscopy trace of the waveguide characterized via sSNOM, and three examples of the third-order near-field signal at 1190, 1160, and 1130 nm, respectively. By averaging over the width of the waveguide, we obtain fringe profiles of the near-field signal at each wavelength (Supplementary Fig. 2b), which are then Fourier transformed to compute the spectral intensity (Supplementary Fig. 2c) [1]. From the spectral intensity, we correlate the observed peaks with a corresponding effective refractive index as $n_{\text{eff}} = q\lambda$, where q is the wave number and λ the free-space wavelength.

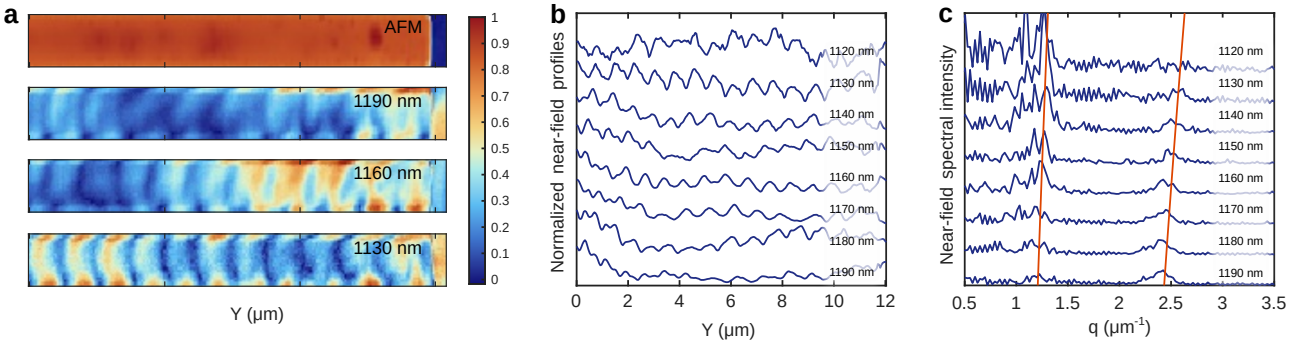

Supplementary Fig. 2. Near-field traces obtained with sSNOM measurements. (a) Atomic force microscopy trace of the probed region and corresponding near-field intensity at three different excitation wavelengths. The depicted region is magnified to show the signal along the width of the examined waveguide and one of the waveguide ends. (b) Extract of the fringe profiles on the WS_2 waveguide in the 1120–1190 nm range measured with sSNOM. (c) Fourier transforms of the profiles, with the two red curves as a guide to the eye, highlighting the effective refractive indices corresponding to the dispersion relation described in Fig. 2f of the main text.

Modelling of out-coupled far-field distribution. Figure 2g of the main text reported the far-field distribution of the fundamental TE mode after coupling out from the designed grating coupler, as obtained with FDTD simulations. Here, we provide additional data for the far-field distribution of the TE_{00} and TM_{00} modes. In particular, Supplementary Fig. 3 presents the far-field distribution of the total electric field, as well as the *p*- and *s*-polarized field. Notably, while the net electric field of the two modes shares a similar pattern, their polarization is inverted, with the TE_{00} mode being s-polarized, and the TM_{00} mode being p-polarized. Given that the polarization-resolved measurements in Supplementary Fig. 9 reveal a *p*-polarized out-coupled field, we can conclude that the main waveguide-coupled mode must have a strong TM component.

Spectral transmittance of WS_2 waveguides. In this note, we report extended data from the transmittance measurements through the 60 μm-long WS_2 waveguide characterized in Fig. 2i of the main text. The transmittance was measured with two spectrometers having charge-coupled device (CCD) cameras optimized for a different wavelength range. Supplementary Figures 4a-b show the transmittance measured with a Horiba iHR 550 spectrometer equipped with a Syncerity BI-NIR camera (Q.E. $>$ 50% between 470 nm–980 nm); in particular, Supplementary Fig. 4b shows the ratio between the spectra obtained with and without grating couplers, revealing two peaks centred around 800 nm and 900 nm providing the largest enhancement.

The transmittance was also probed at room temperature with an infrared-optimized spectrometer equipped with an Andor iDus InGaAs 1.7 μm camera (Q.E. $>$ 50% between 920 nm–1680 nm), showing an additional transmittance peak at 1000 nm for the waveguide with grating couplers, and overall a consistently higher transmittance spectrum over the entire measured range compared to the structure without grating couplers.

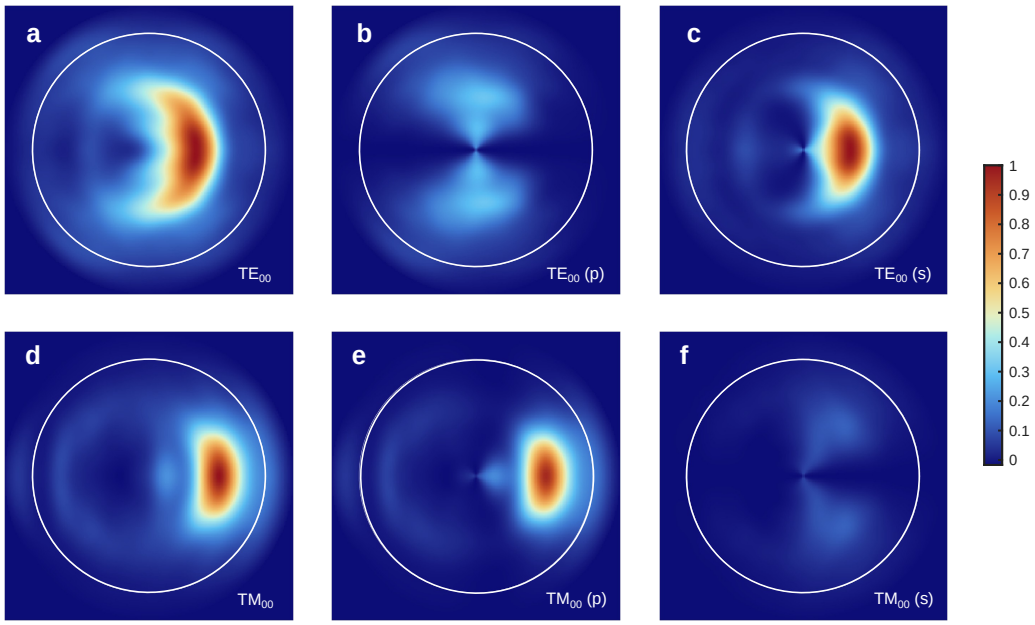

Supplementary Fig. 3. Far-field distributions of the upward-coupled fundamental TE and TM modes at $\lambda = 800$ nm. (a-c) Far-field distribution of the TE_{00} mode for (a) $|E|^2$, (b) $|E_p|^2$, and $|E_s|^2$. (a-c) Far-field distribution of the TM_{00} mode for (a) $|E|^2$, (b) $|E_p|^2$, and $|E_s|^2$. Each field is normalized by maximum $|E|^2$ of the respective mode. The white circle encloses the field of view of an objective with NA = 0.81.

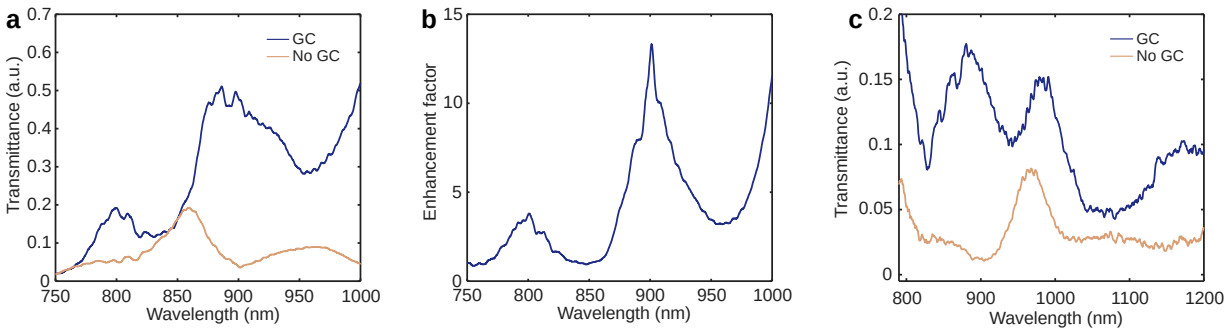

Supplementary Fig. 4. Extended transmittance data. (a) Extended-range transmittance spectra for the 60 µm waveguides characterized in Fig. 2i, with and without grating couplers. (b) Ratio between the transmittance spectrum of the grating-coupled waveguide and the bare waveguide, showing enhancement maxima at 800 nm and 900 nm. (c) Transmittance of the same waveguides in the near-infrared range, measured with an infrared-optimized spectrometer, with and without grating couplers.

Supplementary Note 3: Additional characterization of waveguide-coupled WSe_2 photoluminescence

Photoluminescence imaging of integrated bilayer WSe_2. Supplementary Fig. 5 shows additional photoluminescence imaging of the characterized bilayer, under broadband LED excitation (5a) or under different laser excitation intensities.

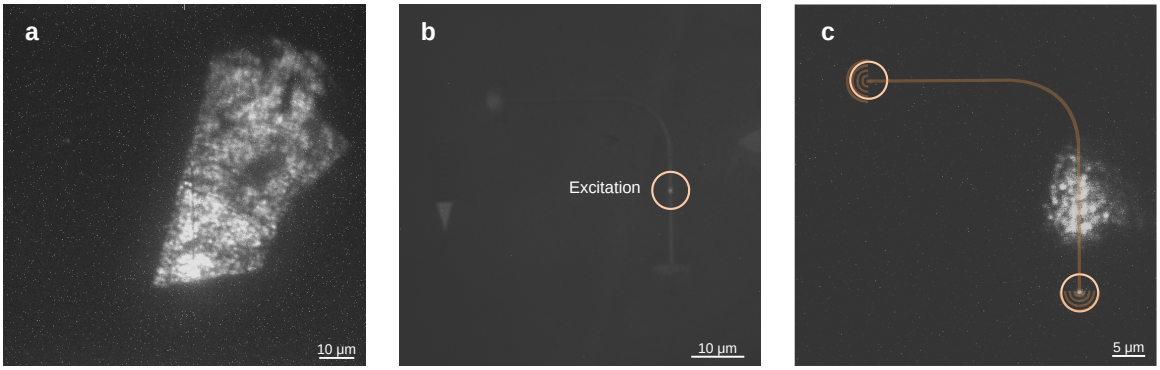

Supplementary Fig. 5. Additional photoluminescence images of the WSe_2 bilayer transferred on a WS_2 waveguide. (a) Photoluminescence of the entire flake under blue LED excitation. (b) Optical image with a dimmed excitation laser on the QE1 emitter (characterized in Fig. 3), with a dimmed infrared LED for structure imaging. (c) Photoluminescence microscopy image under laser excitation of the QE1 emitter.

Power-dependent spectral series. Figure 6 illustrates the spectra as a function of the excitation power under above-band and p-shell excitation, to verify a possible impact of the power-dependent carrier feeding processes on spectral diffusion and emission intensity. In both cases, we did not observe significant spectral broadening or spectral shift as the excitation power increased, suggesting that the increased carrier number had no effect on the spectral diffusion. The initially linear increase in emission intensity and the saturation at higher excitation power reveals the typical saturation behaviour, which is clearly displayed in Fig. 3f in the main text. Moreover, we also observe a clear difference in background emission under the two excitation schemes, where p-shell excitation shows considerably less background emission, even under saturation conditions.

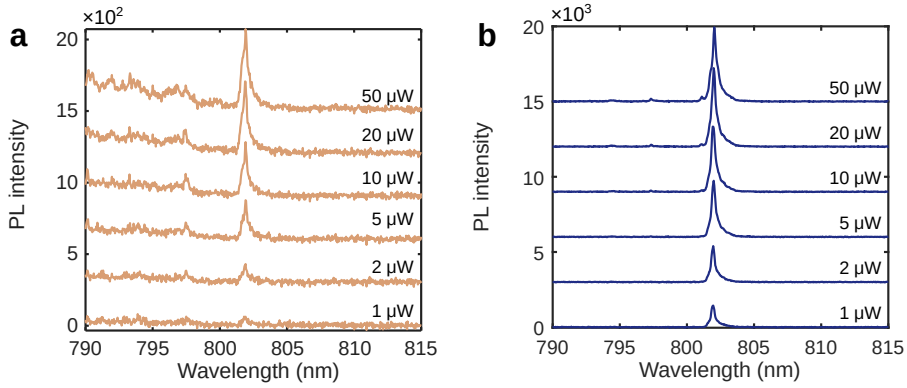

Supplementary Fig. 6. Power-dependent spectra of waveguide-coupled emission under (a) above-band excitation and (b) p-shell excitation. Each spectrum at increasing power is offset by 300 (ABE) or 3000 (PSE) units.

Time-resolved photoluminescence. To verify the dynamics of the investigated emitter QE1, we report time-resolved photoluminescence (TRPL) measurements (Supplementary Fig. 7) under pulsed above-band and p-shell excitation. A mono-exponential fit reveals long—(55.0 ± 1.1) ns under above-band excitation and (31.1 ± 0.4) ns under p-shell excitation—decay time constants. The obtained results could be related to a relatively weak confinement potential, which is affected by the limited WS_2 waveguide-induced strain on the bilayer WSe_2. Another possible cause could be attributed to additional trap states, which significantly affect the emission recombination by slowing down the feeding process of the quantum emitter states. This phenomenon would also justify the observed difference in decay time between the two different excitation schemes. Nevertheless, the decay time constant is long even under p-shell excitation, and further improvements in the efficiency of carrier feeding should be sought for to increase the single-photon emission rate.

Stability of the waveguide-coupled emitter. On top of time-resolved photoluminescence, we also char-

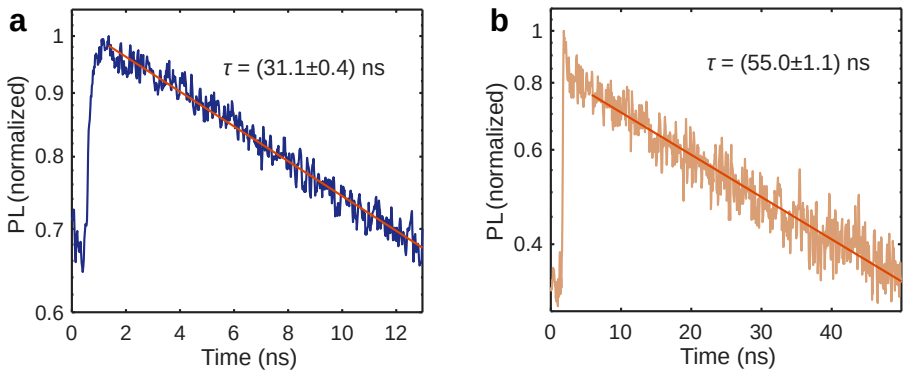

Supplementary Fig. 7. Time-resolved photoluminescence (TRPL) of waveguide-coupled single-photon emission under (a) p-shell excitation and (b) above-band excitation. In addition to reduced background emission and brighter emission, p-shell excitation decreases the decay time of the emitter.

acterized the medium-term stability of the investigated emitter, with particular focus on the variation of its energy state, which is significantly affected by charge noise-driven electrical field fluctuations. Supporting Figure 8 shows a spectrogram of the investigated emitter spectra over a 50 s interval, in which the emission intensity appears to be stable. We observe small fluctuations in the emission peak, which is centred at (801.77 ± 0.12) nm, and its full-width half-maximum linewidth was calculated to be (0.25 ± 0.18) nm. The fluctuation in peak position and the relatively large linewidth suggest a significant effect of spectral diffusion, which could be reduced by applying an electrical bias.

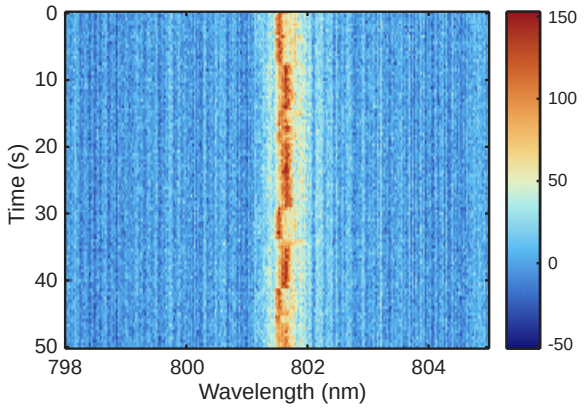

Supplementary Fig. 8. Spectrogram of the waveguide-coupled emitter under p-shell excitation over 50 s, where each spectral snapshot is taken every 250 ms.

Additional polarization-dependent characterization. Figure 3g in the main text revealed a strong degree of linear polarization (DOLP) for emitter QE1, both confocally and at the grating coupler; Supplementary Figure 9a reports the magnified (0.6 nm) spectral data around the peak used to produce those polar plots.

While a strong DOLP in the emitter photoluminescence is observed, no or weak polarization dependence on the emitter brightness is observed when varying the polarization of the excitation source. Supplementary Figure 9b presents the emitter intensity as a function of the polarization of the above-band excitation laser, which is scanned via a half-wave plate to reduce the focused beam movement. Here, the DOLP is limited to $0.14^{+0.25}_{-0.14}$ confocally, and to $0.22^{+0.29}_{-0.22}$, and $0.06^{+0.14}_{-0.06}$ for GC1 and GC2. Under p-shell excitation (Supplementary Fig. 9c), a similarly weak polarization dependence is measured: 0.43 ± 0.20 in the confocal case, decreasing to 0.20 ± 0.06 and 0.15 ± 0.10 at the two grating couplers.

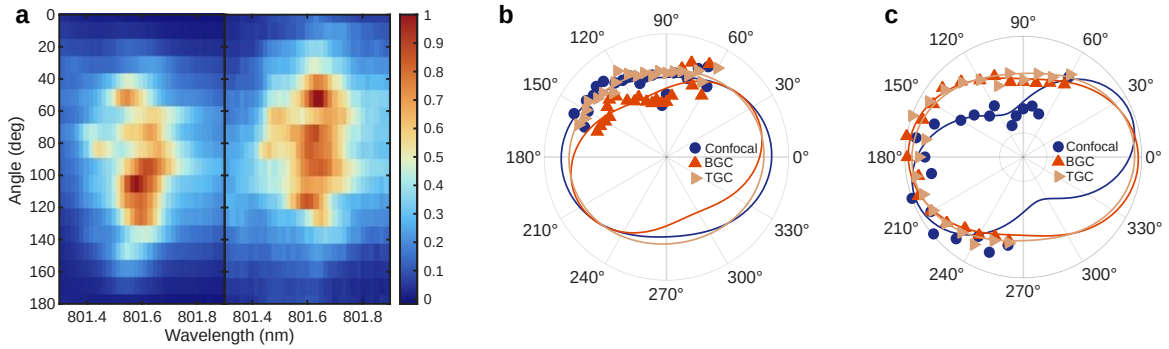

Supplementary Fig. 9. Additional polarization-dependent characterization. (a) Photoluminescence spectra confocal to QE1 (left) and GC1 (right) under p-shell excitation, with variable polarization on the detection arm. (b) Photoluminescence emission against the laser polarization angle under above-band excitation. The DOLP for confocal, GC1, and GC2 is 0.14 ± 0.25, 0.22 ± 0.29, and 0.06 ± 0.14. (c) Photoluminescence emission against the laser polarization angle under p-shell excitation. The DOLP for confocal, GC1, and GC2 is 0.43 ± 0.20, 0.20 ± 0.06, and 0.15 ± 0.10, respectively.

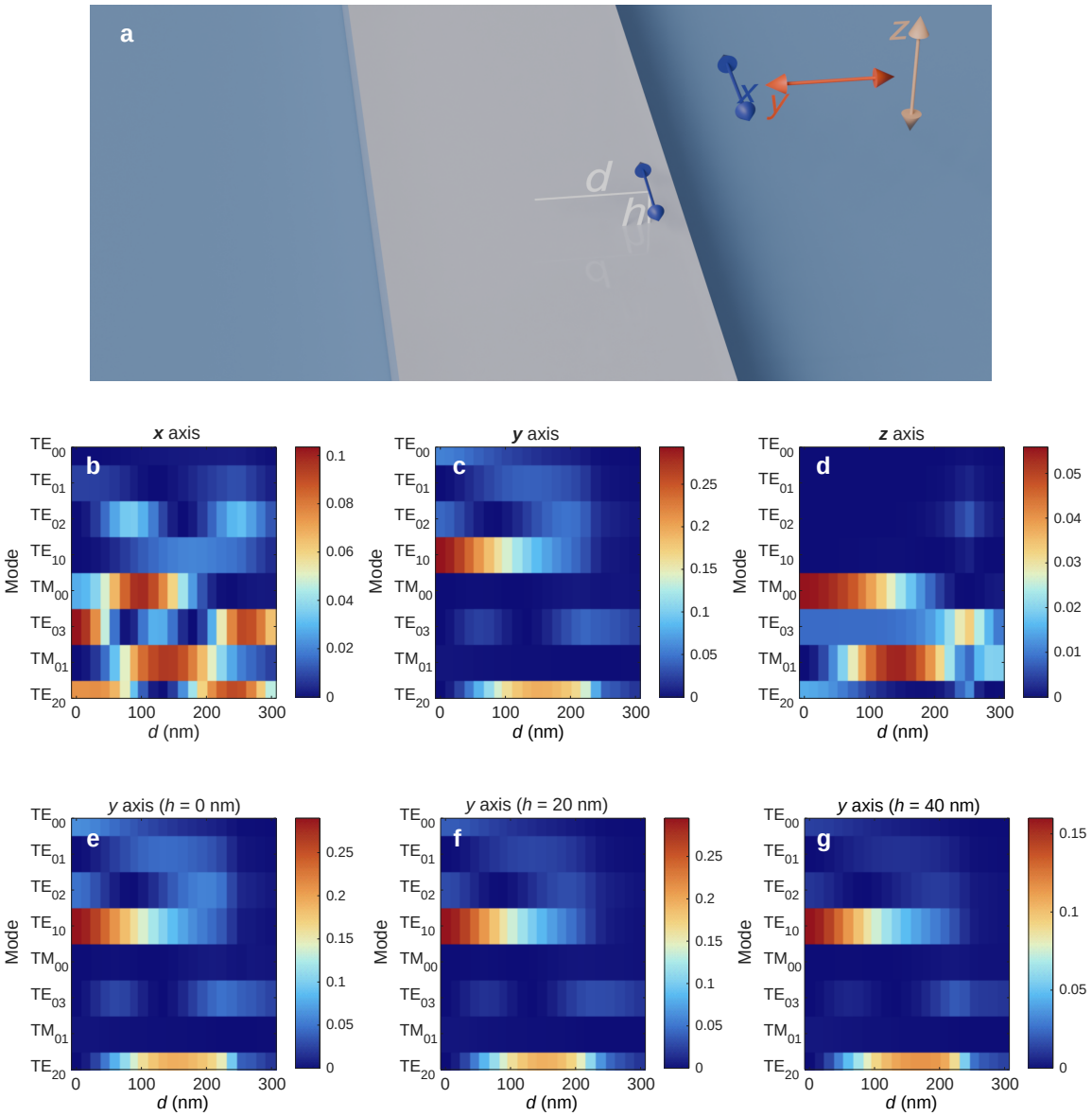

Supplementary Fig. 10. FDTD modelling of the dipole-waveguide coupling efficiency with a dipole placed above the waveguide. (a) Illustration of the model: a dipole is positioned at a height h from the upper surface of the waveguide and a distance d from its vertical symmetry axis; the dipoles are simulated with an orientation along any of the three main axes. (b-d) Coupling efficiency of an electric dipole at $h = 10$ nm and variable d oriented along the (b) x, (c) y, and (d) z axes. (e-g) Coupling efficiency of an electric dipole along the y axis at (e) $h = 0$ nm, (f) $h = 20$ nm, and (g) $h = 40$ nm.

Supplementary Note 4: Modelling of dipole-waveguide coupling efficiency

In this section, we report the coupling of a linearly polarized electric dipole (representing the quantum emitter) to any propagating mode in the waveguide. A FDTD model is built to calculate the mode overlap between the dipole emission and each mode. Since the coupling efficiency is highly dependent on dipole position and orientation, we first sweep the distance d between the vertical waveguide axis and the dipole, with the dipole oriented along the three main axes (Supplementary Fig. 10b-d), while keeping the separation between the dipole and the upper waveguide surface constant to $h = 10$ nm, chosen to reflect a gap due to the middle hBN layer of the sample and a small wrinkle as the origin of strain. Predictably, transverse-electric modes couple better to a y-polarized dipole, but coupling is possible under any dipole orientation because of the higher-order hybrid modes in the waveguide. Since a differently positioned emitter will experience a different mode volume and therefore emit a different power, all the presented results are normalized with the dipole Purcell factor, so that unity emission is assumed under any dipole configuration [2]. Incidentally, modelling the efficiency at different

height for a y-polarized emitter showed little difference in the coupling behaviour over each mode, with only a reduction in maximum coupling efficiency (Supplementary Figs. 10e-g).

We note that there is no implementation of a medium for the very thin WSe_2 and/or hBN flakes on top of the waveguide. An additional medium on the upper surface of the waveguide might increase the maximum coupling efficiency; however, the extreme thickness of the material is likely to make a marginal difference.

In addition to an emitter on top of the waveguide, we consider the case where the emitter originates from a wrinkle on the sides of the waveguide (Supplementary Fig. 11a). Setting the distance d from the waveguide edge to 10 nm, we sweep the height of the dipole (Supplementary Fig. 11b-d). Higher-order TE modes contribute the most to waveguide coupling for in-plane dipoles; conversely, out-of-plane dipole couple better to TM modes or hybrid modes, because of the negligible component of the electric field along the propagation direction in transverse-electric modes. In conclusion, dipoles positioned both on top and on the side of a WS_2 slab waveguide can couple efficiently to a propagating mode–typically of higher order–highlighting the importance of multimode propagation in such an emitter-waveguide configuration.

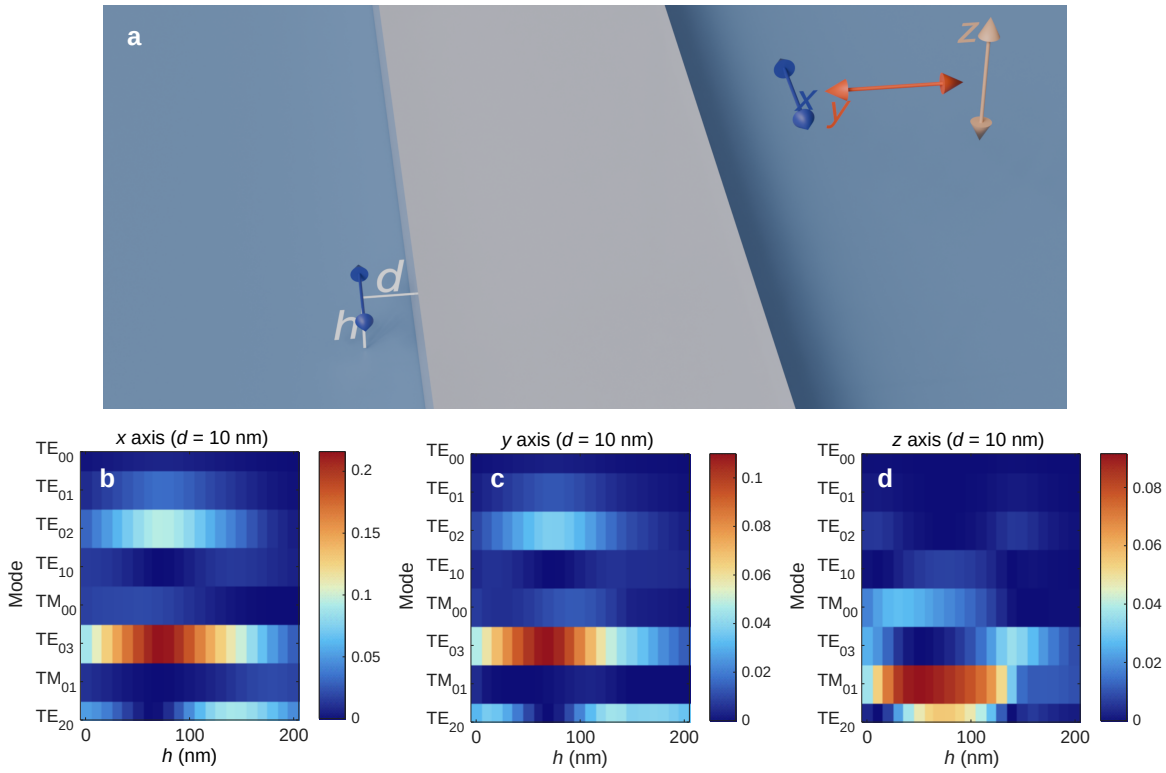

Supplementary Fig. 11. FDTD modelling of the dipole-waveguide coupling efficiency with a dipole placed to the side of the waveguide. (a) Illustration of the model: a dipole is positioned at a distance d from the side of the waveguide and at a height h from the substrate surface; the dipoles are simulated with an orientation along any of the three main axes. (b-d) Coupling efficiency of an electric dipole at $d = 10$ nm and variable h oriented along the (b) x, (c) y, and (d) z axes.

Supplementary Note 5: hBN-free waveguide-emitter coupling

Transferring bilayer WSe_2 on a WS_2 waveguide without a thin hBN layer resulted in a higher likelihood of the flake breaking during the transfer. Supplementary Figure 12a shows an SEM image of a bilayer wrapping around a waveguide, with some minor wrinkle formation and broken edges. The same flake is shown as a whole in another SEM picture in Supplementary Fig. 12b, where the flake is false-colored to highlight it. Despite the flake breaking during the transferring process, PL imaging (performed with a broadband 405 nm LED) shows successful coupling of the emitted light from the WSe_2 flake to the waveguides (see Supplementary Fig. 12c). Following the process for characterizing QE1 presented in the main text, we show an example of waveguide-coupled emitter (QE4) at around 800 nm under above-band excitation, showing rather limited intensity and significant linewidth (see Supplementary Fig. 12d).

Time-resolved photoluminescence under pulsed above-band excitation showed a long decay time ($\tau = (22.58 \pm 1.98)$ ns; see Supplementary Fig. 12e), albeit shorter than QE1. Again, this can be attributed to a relatively slow carrier feeding process or a weak dipole oscillatory strength. Despite the considerably lower brightness in this emitter, its emission was confirmed to be of single photons with a second-order autocorrelation measurement (Supplementary Fig. 12f), where $g^{(2)}(0) = 0.294 \pm 0.036$, supporting the observation of waveguide-coupled quantum emitters on hBN-free WSe_2/WS_2 photonic circuits.

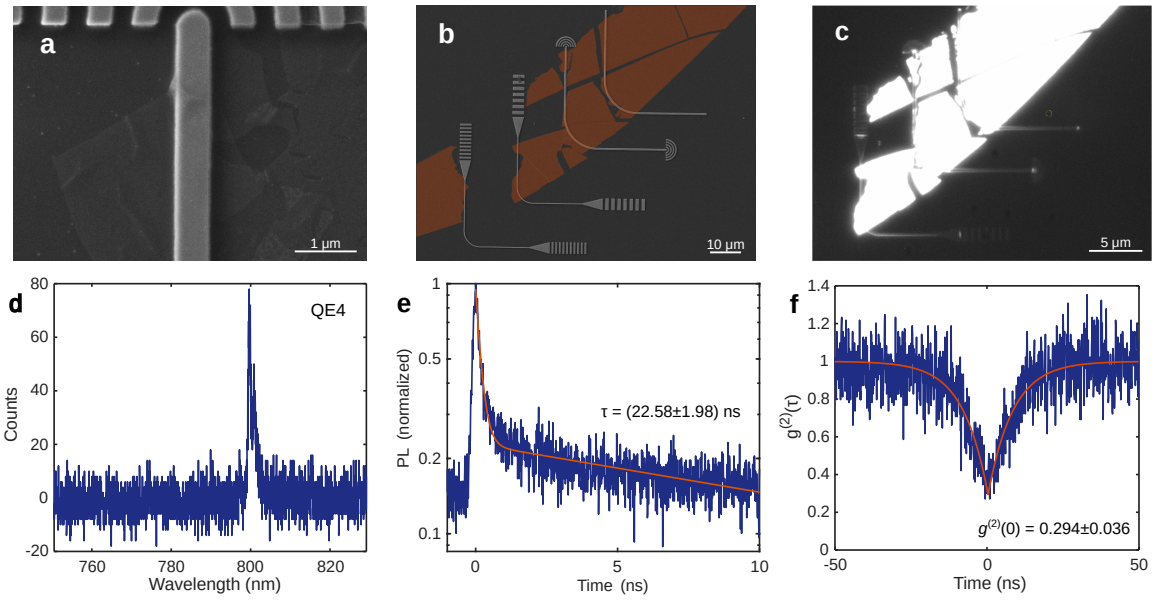

Supplementary Fig. 12. Characterization of a WSe_2 directly transferred on a WS_2 waveguide. (a) SEM image of a detail of the transferred flake on the waveguide. (b) SEM image of the entire bilayer; the bilayer flake is false-colored in orange. (c) Photoluminescence image of the bilayer under blue LED illumination. (d) Photoluminescence spectra of a waveguide-coupled emitter, collected at a grating coupler, under above-band excitation. (e) Time-resolved photoluminescence of the emitter in (d); the decay time is extracted from the slower constant in a double-exponential fit. (f) Second-order autocorrelation of the emitter, measured in confocal configuration.

Supplementary Note 6: Extended second-order correlation traces

In this note, we present extended data for single-photon emission characterization, which shows a mild photon-bunching effect originating from luminescence blinking and likely a consequence of charge fluctuations [3]. Supplementary Figure 13a-c shows the autocorrelation function $g^{(2)}(\tau)$ measurements results ranging from -2 µm to 2 µm for all configurations presented in the main text (see Fig. 4 in the main text). From these histograms, we conclude that the effect of bunching is limited, as already mentioned in the main text, to a scale of up to ± 50 ns, which suggests the absence of longer-scale blinking processes. Moreover, the limited bunching amplitude (0.08 ± 0.02, 0.19 ± 0.01, and 0.15 ± 0.01 in Supplementary Fig.s 13a, b, and c, respectively) being less than 0.20 after normalization implies the presence of non-radiative recombination processes, setting an upper limit of the internal quantum efficiency to $\eta_i \leq 1/((1+A_\mathrm{b}) = 0.84$ [4, 5]. Incidentally, the raw $g^{(2)}(0)$ values from the histogram are 0.0576, 0.0161, and 0.0777, for the setup of Supplementary Fig. 13a, b, and c, respectively. All these results underscore the high quality of the investigated emitter in terms of purity and brightness, which could be further improved by better charge noise mitigation, such as through electrical stabilization or resonant excitation.

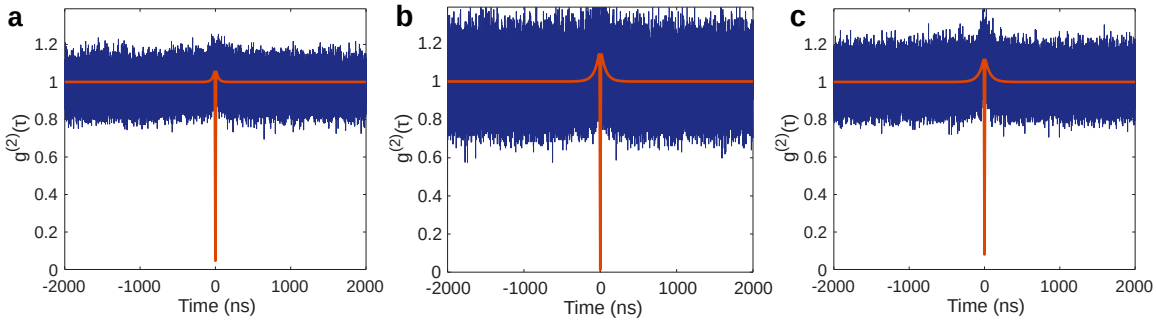

Supplementary Fig. 13. Extended second-order autocorrelation histograms with (a) the collection spot confocal to the excitation source, (b) the collection spot at one grating coupler, and (c) two collection spots at each grating couplers; the traces were processed with a three-point moving average, and show the extinction of photon bunching within the presented range.

Supplementary Note 7: Coupling efficiency of the quantum emitter

In this note, we estimate the waveguide-coupled single-photon emission rate and the coupling efficiency for emitter QE1. The detection rate at the superconducting-nanowire single-photon detector (SNSPD) can be modelled as

$$R = R_{\mathrm{d}} + \eta_{\mathrm{det}}\eta_{\mathrm{opt}}\eta_{\mathrm{gc}}\eta_{\mathrm{pr}}\eta_{\mathrm{wg}}(R_{\mathrm{em}} + R_{\mathrm{bg}}), \tag{1}$$

where R_{d} is the dark count rate, η_{det} the detector efficiency at 802 nm, η_{opt} the total transmission efficiency through the experimental optical setup, η_{gc} the out-coupling efficiency from the grating coupler, η_{pr} is the propagation efficiency along the waveguide, η_{wg} is the emitter-waveguide coupling, R_{em} is the total single-photon emission rate, and R_{bg} is the background emission rate.

In order to estimate the emitter-waveguide coupling efficiency η_{wg}, we measure the transmission of each optical element used in our second-order autocorrelation measurements with the SNSPD, as shown in Supplementary Table I. This results in a total transmission efficiency of $\eta_{\mathrm{opt}} = 0.134$. Moreover, we use the maximum estimate grating coupler efficiency at the operating wavelength (0.188 for the TM_{00} mode) to determine the lower bound of waveguide-coupled single photons, as explained later in this section.

Optical element	Efficiency
Objective and cryostat windows (optimal)	0.73
Beam splitters and polarization optics (optimal)	0.51
Filtering and fibre coupling efficiency (estimated)	0.40
Fibres and connectors	0.90
Total optical setup η_{opt}	0.134
Detector efficiency (optimal) η_{det}	0.50
Modelled grating coupler efficiency at 802 nm η_{gc}	≤ 0.188
Decay time (TRPL)	31.1(4) ns

TABLE I. Experimental and theoretical parameters used for the calculation of the collection and extraction efficiency.

We remark that the background reduction obtained under p-shell excitation and the filtering with a tuneable longpass and bandpass filter (with a FWHM of ≈ 10 nm) lead to a very high measured purity in QE1 ($g^{(2)}(0) = 0.003^{+0.030}_{-0.003}$ at the upper grating coupler). Furthermore, the dark count rate measured by the SNSPD is negligible ($R_d < 10$ Hz). Therefore, we can consider the detection rate at the SNSPD as a single-photon detection rate, that is

$$R \approx \eta_{\mathrm{det}}\eta_{\mathrm{opt}} \underbrace{\eta_{\mathrm{gc}} \overbrace{\eta_{\mathrm{pr}}\eta_{\mathrm{wg}}R_{\mathrm{em}}}^{R_{\mathrm{wg}}}}_{R_{\mathrm{L}}}. \tag{2}$$

Starting from the upper grating coupler (GC1), where the single-photon rate at saturation is $R_1 \approx 20$ kHz under CW p-shell excitation, we first determine the single-photon emission rate at the first lens by removing the detection and transmission losses. This results in a single-photon rate at the first lens of $R_{\mathrm{L1}} \approx 299$ kHz. The same calculation is repeated with the detection rates measured at the lower grating coupler (GC2; $R_2 \approx 15$ kHz) and under confocal collection ($R_{\mathrm{c}} \approx 100$ kHz), resulting in $R_{\mathrm{L2}} \approx 223$ kHz and $R_{\mathrm{Lc}} \approx 1\,490$ kHz, respectively.

To determine the single-photon rate inside the waveguide, the out-coupling efficiency losses must be subtracted. However, the exact grating coupler efficiency η_{gc} is not accessible, as it varies for each propagating mode, and we do not have access to the mode distribution of the waveguide-coupled single-photon emission. Therefore, we use the maximum out-coupling efficiency obtained with FDTD modelling (corresponding to 18.8%). This provides an upper bound on the waveguide-coupled single-photon emission, which is in all likelihood higher than what we report here, due to both fabrication imperfections and multimode propagation reducing the actual grating coupler efficiency. By summing single-photon rate for both grating coupler arms, we obtain a waveguide-coupled single-photon rate of $R_{\mathrm{wg}} \gtrsim 2.78$ MHz. Incidentally, we remark that the estimated waveguide-coupled single-photon rate includes propagation losses η_{pr} over a length of 60 µm.

We conclude by drawing some conclusions regarding the emitter brightness and the emitter-waveguide coupling efficiency. The calculation of the confocal extraction efficiency is limited by the use of a CW excitation source, which could not be avoided because of the decay time of the emitter (31.1 ns) exceeding the minimum

pulse separation of our laser (12.5 ns). Assuming an internal quantum efficiency of 0.84 (the upper limit obtained from the second-order autocorrelation function with the strongest bunching; see Supplementary Note 6), the maximum emission rate would be limited by the decay time and correspond to $R_{\mathrm{exc}} = 27.0$ MHz. In this case, the emitter-waveguide coupling efficiency would be $R_{\mathrm{wg}}/R_{\mathrm{exc}} \gtrsim 0.10$, and the confocal extraction efficiency would be 0.06.

Single-photon detection rate, GC1 (kHz)	20
Single-photon detection rate, GC2 (kHz)	15
Single-photon detection rate, confocal (kHz)	100
First-lens single-photon rate, GC1 (kHz)	299
First-lens single-photon rate, GC2 (kHz)	223
First-lens single-photon rate, confocal (kHz)	1 490
Total waveguide-coupled single-photon rate (kHz)	$\gtrsim$ 2 780
Maximum emission rate (kHz)	27 000
Emitter-waveguide coupling efficiency	$\gtrsim$ 0.10
Confocal extraction efficiency	0.06

TABLE II. Summary of the estimated values for single-photon rates and quantum efficiency.

[1] Casses, L. N.; Zhou, B.; Lin, Q.; Tan, A.; Bendixen-Fernex de Mongex, D.-P.; Kaltenecker, K. J.; Xiao, S.; Wubs, M.; Stenger, N. Full Quantitative Near-Field Characterization of Strongly Coupled Exciton–Plasmon Polaritons in Thin-Layered WSe2 on a Monocrystalline Gold Platelet. *ACS Photonics* **2024**, *11*, 3593–3601.

[2] Wang, Y. J.; Vannucci, L.; Burger, S.; Gregersen, N. Near-Unity Efficiency in Ridge Waveguide-Based, on-Chip Single-Photon Sources. *Mater. Quantum. Technol.* **2022**, *2*, 045004.

[3] Paralikis, A.; Wyborski, P.; Metuh, P.; Gregersen, N.; Munkhbat, B. Tunable and Low-Noise WSe2 Quantum Emitters for Quantum Photonics. *PRX Quantum* **2025**, *6*, 040339.

[4] Kim, J.; Kaupp, J.; Reum, Y.; Peniakov, G.; Michl, J.; Kohr, F.; Emmerling, M.; Kamp, M.; Cho, Y.-H.; Huber-Loyola, T.; Höfling, S.; Pfenning, A. T. Two-Photon Interference from an InAs Quantum Dot Emitting in the Telecom C-Band. *Advanced Quantum Technologies* **2025**, *8*, e2500069.

[5] Vajner, D. A.; Holewa, P.; Zieba-Ostój, E.; Wasiluk, M.; von Helversen, M.; Sakanas, A.; Huck, A.; Yvind, K.; Gregersen, N.; Musiał, A.; Syperek, M.; Semenova, E.; Heindel, T. On-Demand Generation of Indistinguishable Photons in the Telecom C-Band Using Quantum Dot Devices. *ACS Photonics* **2024**, *11*, 339–347.